crystals

MDPI

Article

How the Hinge Region Affects Interactions between the Catalytic and β-Propeller Domains in Oligopeptidase B

Vladimir I. Timofeev [1,2,3,*,†], Yury A. Gaponov [1,†], Dmitry E. Petrenko [1], Georgy S. Peters [1], Yulia K. Agapova [1], Alena Y. Nikolaeva [1], Anna G. Mikhailova [3] and Tatiana V. Rakitina [3,*]

[1] National Research Center "Kurchatov Institute", 123182 Moscow, Russia; gaponov_ya@nrcki.ru (Y.A.G.); dmitry.e.petrenko@gmail.com (D.E.P.); georgspeters@gmail.com (G.S.P.); agapova.jk@gmail.com (Y.K.A.); nikolaeva_ay@nrcki.ru (A.Y.N.)
[2] Federal Scientific Research Center "Crystallography and Photonics", Russian Academy of Science, 119333 Moscow, Russia
[3] Shemyakin-Ovchinnikov Institute of Bioorganic Chemistry, Russian Academy of Science, 117997 Moscow, Russia; anna.g.mikhailova@gmail.com
* Correspondence: tostars@mail.ru (V.I.T.); taniarakitina@yahoo.com (T.V.R.)
† These authors contributed equally to this work.

Abstract: In order to elucidate the effect of modification of the hinge region on structural polymorphism associated with conformational transitions, structural studies of hinge-modified oligopeptidase B from *Serratia proteamaculans* (SpOpBmod) in the crystalline state and solution were carried out. A new crystal structure of SpOpBmod in the intermediate conformation was obtained, and a molecular model of SpOpBmod in the open conformation was created using a combination of small-angle X-ray scattering with MD simulations. The improved electron density of the mobile H-loop carrying the catalytic H652 distinguished the obtained crystal structure from that which was previously reported. Good electron density in this region was previously found only in the inhibitor-bound SpOpBmod structure, in which one of the inhibitor molecules was covalently bound to H652. Comparison of the above structures of free and inhibitor-bound enzymes showed that both tertiary folds are the result of the internal conformational dynamics of SpOpBmod, which were captured by inhibitor binding. Comparison of the SpOpBmod structures with the structures of the same enzyme with a native hinge peptide made it possible to establish the influence of hinge modification on the rearrangement of the interdomain interface during conformational transitions. The above analysis also used models of native and hinge-modified enzymes in open conformations. We found that the interdomain interface observed in the crystal structures of hinge-modified enzymes could be considered an extreme version of the H-loop arrangement, in which closure of the domains does not lead to the assembly of the catalytic triad, whereas the intermediate conformation observed in the structure of the enzyme with the native hinge sequence illustrates a productive transition to the catalytically active closed conformation.

Keywords: prolyloligopeptidase; oligopeptidase B; multidomain proteins; structural polymorphism; conformational transitions; hinge region; interdomain interface; β-propeller

Citation: Timofeev, V.I.; Gaponov, Y.A.; Petrenko, D.E.; Peters, G.S.; Agapova, Y.K.; Nikolaeva, A.Y.; Mikhailova, A.G.; Rakitina, T.V. How the Hinge Region Affects Interactions between the Catalytic and β-Propeller Domains in Oligopeptidase B. *Crystals* **2023**, *13*, 1642. https://doi.org/10.3390/cryst13121642

Academic Editor: Abel Moreno

Received: 12 October 2023
Revised: 20 November 2023
Accepted: 25 November 2023
Published: 27 November 2023

1. Introduction

In the modern world, a number of the most important biotechnological and pharmacological tasks are solved using computational biology and huge datasets of structural information about biological macromolecules and their complexes collected in specialized databases, such as the Protein Data Bank (PDB, https://www.rcsb.org/ accessed on 1 October 2023). Crystal structures serve as the most reliable basis for computer modeling due to their exceptionally high (up to atomic) resolution [1]. The range of tasks solved in silico on the basis of structural data extends from the creation of enzymes with required activities and/or operational stabilities to the modeling of small molecule inhibitors specific

to certain proteins, usually enzymes, whose altered expression and/or mutations cause severe diseases, including cancer and diabetes [2]. Targeted therapy was developed based on such inhibitors. Today, the most common are competitive inhibitors that interact with the substrate-binding site of the enzyme and prevent the substrate from accessing it, while allosteric inhibitors are less common but not less promising [3,4]. Allosteric inhibitors bind to target proteins outside the substrate-binding pockets and affect the molecular conformational dynamics, causing—for example—stabilization of the enzymes in a catalytically inactive conformation [5,6].

To date, conformational transitions between catalytically active and catalytically inactive conformations have been described for many enzymes. In particular, conformational variability is characteristic of multi-domain proteins, which often contain flexible interdomain linkers, also called hinge regions [7]. One example of such enzymes is the two-domain prolyloligopeptidases (POPs), which constitute the S9 family of serine proteases from the SC clan [8–10]. This family includes several subfamilies containing enzymes with different substrate specificities but similar two-domain architecture (Figure 1).

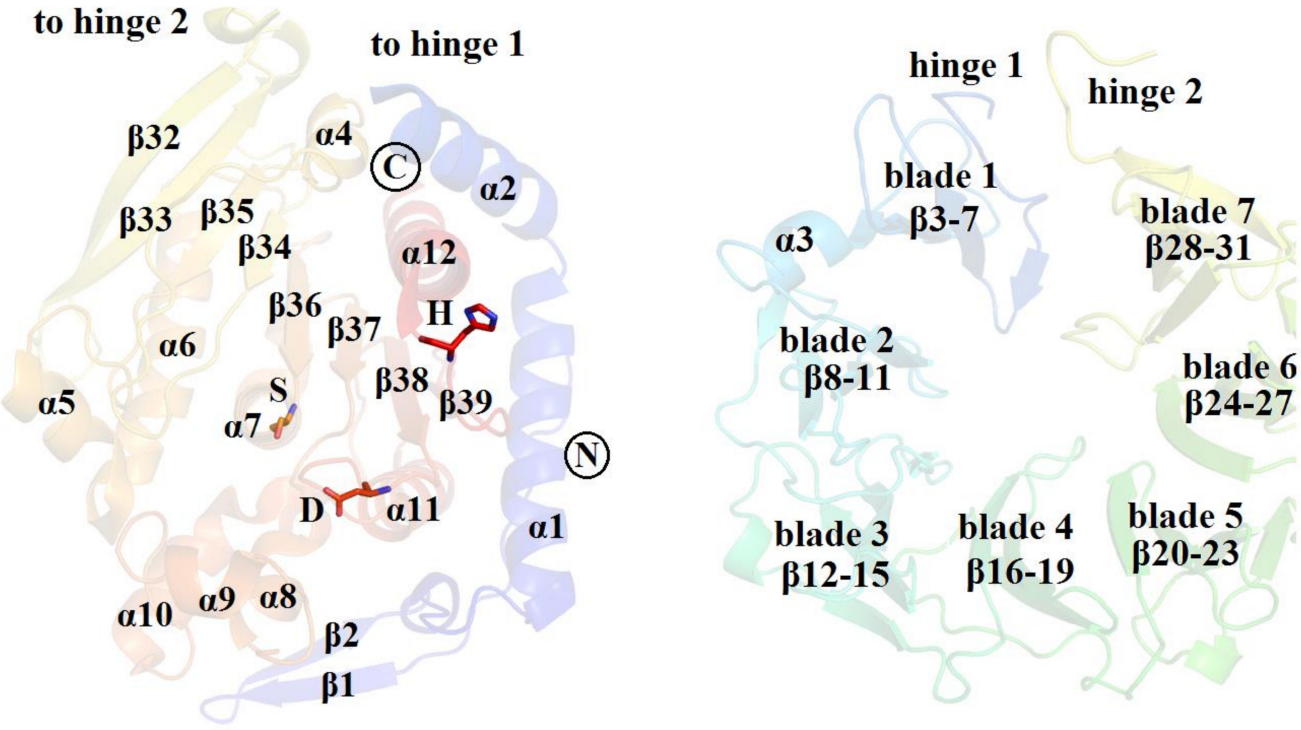

Figure 1. Semitransparent cartoon images of the catalytic (**left**) and β-propeller (**right**) domains of POP family enzymes. View from inside the interdomain cavity. The two hinge peptides connecting the domains and secondary structure elements are labeled. The color coding is in the rainbow style: N-terminus (N) is blue, C-terminus (C) is red. The catalytic domain includes an N-terminal loop (colored blue) and an α/β hydrolase fold (colored from yellow to red) with the catalytic triad residues (S, D, and H) shown in sticks. The β-propeller domain (colored from blue to yellow) has an open-Velcro topology. The crystal structure of SpOpBmod (PDB ID 7YWZ) was used to prepare this figure.

All POPs consist of an α/β-hydrolase catalytic domain containing all the residues of the catalytic triad (S, D, and H) and a regulatory β-propeller domain, which serves to limit the size of potential substrates and connects to the catalytic domain through a hinge region consisting of two peptides with a size of about seven amino acid residues [8,10,11]. It has been shown that in most enzymes of the POP family, domains can converge and move away from each other. In addition to these domain movements, local (intradomain) rearrangements occur, causing the assembly and disassembly of the catalytic triad, which

depends primarily on the movements of the long and flexible loop carrying the catalytic residue H (H-loop) [12–14].

Structural variability due to different arrangements of both domains and residues of the catalytic triad was first discovered by analyzing crystal structures. An open conformation, in which the interdomain cavity is enlarged and the catalytic triad is disrupted, was found in crystals of ligand-free POPs of bacterial origin and OpB from *Trypanosoma brucei* [12–14]. Small-angle X-ray scattering (SAXS) studies confirmed the predominance of the open conformation in solution of bacterial OpB from *Serratia proteamaculans* (SpOpB) [15].

A closed conformation, in which the catalytic triad is assembled and the domains are closed, has been found in crystals of inhibitor-bound POPs from bacteria and OpBs from protozoa [12–14,16,17]. Mammalian POPs (both free and inhibitor-bound) always crystallize in the closed conformation [11,18], although a number of studies have suggested that mammalian POPs also exhibit conformational transitions similar to those observed in bacterial POPs [19–21].

An intermediate conformation, in which domain closure was not accompanied by assembly of the catalytic triad, was first discovered in the crystal structure of the archaeal POP from *Pyrococcus furiosus* with a prolyl-proline moiety in the interdomain cavity [22]. Later, using X-ray diffraction and SAXS analysis, we showed that SpOpB adopts the intermediate conformation in the presence of spermine [15].

In [15] and subsequent structural studies [23,24], we used mutant derivatives of SpOpB in most of which the amino acid sequence of the first hinge peptide (IPQQEH) was replaced by a TEV protease site (ENLYFQ). The significantly decreased catalytic efficiency of SpOpBmod compared to SpOpB (a wild-type enzyme with a native hinge peptide) was shown in [15]. These results supported the previously postulated idea that targeting the structural dynamics of domain closing and opening using the hinge region could be a successful strategy for manipulating the catalytic activity of OpB and other POPs [14].

To elucidate the mechanism of the hinge-dependent loss of SpOpB activity, we compared the available structures of the enzyme with the native and modified hinge region [24]. We found that the modification was associated with the formation of an interdomain salt bridge (SB) between the side chains of the catalytic residue D617 and R151 from the β-propeller domain. This SB caused the stabilization of D617 itself and its entire loop (D-loop) in a position that prevented the movement of the H-loop from the periphery to the center of the interdomain cavity [24].

In this work, we addressed the question of why modification of the first hinge peptide sequence results in the formation of the above-mentioned interdomain SB between D617 and R151. We assumed that the appearance of this SB is the result of a rearrangement of the network of interdomain contacts. To describe this rearrangement in detail, we used new results obtained from structural studies of SpOpBmod in the crystalline state and solution. A crystal structure of SpOpBmod in the intermediate conformation with improved electron density in the H-loop region and a SAXS-validated molecular model of SpOpBmod in the open conformation were obtained and compared to similar structures of the enzyme with an unmodified hinge.

2. Materials and Methods

2.1. Production of the Recombinant Protein

SpOpBmod-expressing plasmid was obtained as described in [15]. Rosetta(DE3)pLysS *E. coli* cells (Novagen, Darmstadt, Germany) transformed with the plasmid were grown in LB medium supplemented with 100 μg/mL ampicillin and 34 μg/mL chloramphenicol at 37 °C until the OD600 value reached 0.8. Then, the expression was induced with 0.2 mM IPTG and the cells were incubated at 25 °C for 16 h. After harvesting via centrifugation (5000× *g*, 10 °C, 20 min), the cells were solubilized in 50 mM Tris-HCl buffer supplemented with 500 mM NaCl, 20 mM imidazole 0.02% (*v*/*v*) Triton X-100, and 1 mM PMSF (pH 8.0) and further disrupted by sonication. The crude cell lysate was centrifuged (20,000× *g*, 10 °C, and 30 min). The supernatant was loaded onto a 5 mL Ni-NTA Superflow Cartridge

(Qiagen, Venlo, The Netherlands) equilibrated with 50 mM Tris-HCl buffer supplemented with 500 mM NaCl, and 20 mM imidazole (pH 8.0). After washing with 50 mM Tris-HCl buffer supplemented with 500 mM NaCl and 40 mM imidazole (pH 8.0), recombinant SpOpBmod was eluted with 20 mM Tris-HCl buffer supplemented with 200 mM NaCl and 300 mM imidazole (pH 8.0). All purification steps were carried out at 15 °C and controlled via sodium dodecyl-sulfate polyacrylamide gel electrophoresis (SDS-PAGE). SpOpBmod-containing protein fractions were combined; protein concentration was determined by Bradford method. The 30 kDa cutoff centrifugal filter devices (Millipore, Burlington, MA, USA) were used for buffer exchange and protein concentration.

2.2. Crystallography, X-ray, and Structural Analysis

Crystallization of SpOpBmod (21 mg/mL in 20 mM Tris-HCl buffer supplemented with 100 mM NaCl (pH 8.0)) was carried out in the presence of 5 mM spermine [25]. Crystals were grown at 4 °C in 0.2 M $(NH_4)_2SO_4$, 0.1 M MES pH 6.5, and 30% PEG-5000. Paraton was used as a cryoprotectant. Diffraction data were collected at the SPring-8 synchrotron facility (Harima Science Garden City, Kamigori, Japan). Diffraction data were obtained from one crystal using the rotation method. Rocking and rotation angles are 0.1° and 360°, respectively. A DECTRIS EIGER X 16 M detector (Dectris, Baden, Switzerland). Twas used to record reflections. The set of experimental reflection intensities was processed using the iMosflm program [26]. The structure was solved by the molecular replacement method using the BALBES program [27]. Refinement, visual evaluation of the electron density map, and manual rebuilding of the model were performed with the REFMAC5 program of the CCP4 suite [28] and the COOT interactive graphics program [29], respectively. Visual inspection of the structure and analysis of the interdomain interface were performed using either the COOT program [29], PyMOL Molecular Graphics System, Version 1.9.0.0 (Schrödinger, New York, NY, USA) or PDBePISA [30]. Superpositions of the structures were carried out using the LSQKAB program [31]. Statistics of the data collection and refinement are collected in Table 1.

Table 1. Data collection, processing, and refinement.

PDB ID **Protein**	**7YWZ** **SpOpBmod**
Data Collection	
Diffraction source	SPring-8
Wavelength (Å)	0.8
Temperature (K)	100
Detector	DECTRIS EIGER X 16 M
Space group	$P2_12_12_1$
a, *b*, *c* (Å)	72.89, 100.44, 108.55
α, β, γ (°)	90.0
Unique reflections	76,338
Resolution range (Å)	29.51–1.75 (1.80–1.75)
Completeness (%)	99.50 (99.93)
Average redundancy	4.96 (4.87)
$\langle I/\sigma(I) \rangle$	7.4706 (2.53)
Rmrgd-F * (%)	6.6 (29)
Willson B	18.3
Refinement	
Rfact (%)	17.3
Rfree (%)	20.2
Rfree set size (%)	5

Table 1. *Cont.*

PDB ID **Protein**	**7YWZ** **SpOpBmod**
Refinement	
RMSD of bonds (Å)	0.011
RMSD of angles (°)	1.73
Ramachandran plot	
Most favored (%)	99.6
Allowed (%)	0.4
No. atoms	
Protein	5545
Water	562
Ligands	62
B-factor (Å2)	
Average	22.0

Values in parenthesis are for the highest-resolution shell. * $Rmrgd - F = 2\sum_{hkl}|\langle I_1(hkl)\rangle - \langle I_2(hkl)\rangle|/\sum_{hkl}\langle I_1(hkl)\rangle - \langle I_2(hkl)\rangle$ [32].

2.3. SAXS Experiment

SAXS experimental data were collected at the BioMUR beamline of the specialized synchrotron radiation source Kurchatov of the National Research Center "Kurchatov Institute", Moscow, Russia. The focusing optical scheme with DECTRIS Pilatus3 1M area detector (Dectris, Baden, Switzerland) was used at the beamline. The energy of the synchrotron radiation beam at the beamline was fixed Ebeam = 8 keV. The sample-to-detector distance was 0.98 m. A sample of silver behenate powder was used as the calibration standard for all SAXS experiments.

Protein was dissolved in the buffer (20 mM Tris-HCl, 100 mM NaCl, pH 8.0) and concentrated to 4 mg/mL with the 30 kDa cutoff centrifugal filter devices (Millipore, Burlington, MA, USA). The flowthrough from the concentrator was used as a buffer control. Samples were placed in quartz capillaries with 2 mm diameters. Measurements were performed at room temperature with an exposure time of 600 s. SAXS experimental data were reduced and primarily processed using FIT2D and ATSAS software [33,34].

2.4. MD Simulation and Analysis of MD Trajectories

Starting structures for MD simulation of all three conformations of SpOpBmod were obtained as described below.

As a starting model for the intermediate conformation of SpOpBmod, we used the crystal structure of SpOpBmod in complex with Na-p-Tosyl-Lysyl Chloromethylketone (TCK) (PDB ID 7NE7, [23]) without TCK and spermine molecules.

As a starting model for the closed conformation of SpOpBmod, we used the crystal structure of SpOpB in a complex with TCK (PDB ID 7YWP, [17]), without TCK, and with the replacement of the first hinge peptide sequence with the sequence of the TEV protease site.

As a starting model for the open conformation of SpOpBmod, we used the model of the SpOpB open conformation obtained through combination of classical MD dynamics and essential sampling in [24], in which the first hinge peptide sequence was replaced by that of the TEV-protease site.

MD simulations were carried out using the GROMACS 2020.3 software package [35] and the AMBER99SB-ILDN force field [36]. All three starting structures were solvated with water of the SPC/E type in a periodic rectangular box with a 1.0 nm distance between the solute and the box. The charge of the system was neutralized by complementing the solvent with Na^+ и Cl^- ions. The standard protocol of simulation was used for the system equilibration. To relax the structure and avoid steric collisions during further modeling, the potential energy was minimized with an increment of 1 fs to a maximum force of 1000.0 kJ/mol/nm. The pressure and temperature were stabilized at 1 atm and 300 K using NVT (100 ps) and NPT (100 ps) simulations, respectively. The pressure and temperature in

the system were maintained independently at the same level using a modified Berendsen thermostat [37] and a Parinello–Rahman barostat [38], respectively. Long range electrostatic interactions were calculated using the Particle Mesh–Ewald summation scheme [39]. The LINCS algorithm was used to limit bonds involving hydrogen atoms [40]. Finally, three productive 100 ns MD simulations were performed with the data collection at every 10 ps.

The changes in the protein folding along the MD trajectories were evaluated by calculating the root mean square deviations (RMSD) for the backbone atoms. Clustering of the structures obtained during simulation was performed using GROMACS subprograms.

2.5. Comparison of the SAXS Experimental Data with Calculated SAXS Curves

First, all three starting models, energy-minimized starting models (t = 0 ns), and models representing the main structural clusters for each MD trajectory were processed to generate model SAXS curves, which were fitted to the experimental SAXS curve using CRYSOL3.0 software [41]. Radius of gyration (Rg) was calculated using Equation (1) [42].

$$Rg = \sqrt{\sum_i m_i r_i^2 / \sum_i m_i}\,, \quad (1)$$

where m_i is the mass of the atom with index i, $r_i = R_i - R_{cm}$, R_i is the radius vector of the atom with index i, and R_{cm} is the radius vector of the center of mass of the macromolecule or domain, which is calculated using Equation (2).

$$R_{cm} = \sum_i m_i R_i / \sum_i m_i\,. \quad (2)$$

The experimentally calculated Rg values within the calculation errors coincided with those calculated using the CRYSOL3.0 software.

After confirming the open conformation of SpOpBmod in solution, the corresponding MD trajectory was used to search for the best model among the structural invariants distributed along the MD trajectory.

OpBs consist of two domains connected by hinge peptides. For this reason, in addition to the standard fitting criteria reduced chi-square (χ^2), Rg and Dmax (maximum distances between two atoms of a molecule, calculated from atomic coordinates), additional parameters were used to evaluate the structural invariants generated along the MD trajectory, namely, the interdomain distances (Did) and Rg of the separated domains (R1g) and (R2g).

2.6. Data Bank Accession Numbers

The structure of SpOpBmod has been deposited into the Protein Data Bank (PDB) under accession code 7YWZ.

3. Results and Discussion

3.1. Crystal Structure of SpOpBmod in the Intermediate Conformation with an Improved Electrone Density in the H-Loop Region

A new crystal structure of SpOpBmod (PDB ID 7YWZ) was determined at 1.75 Å resolution (Table 1, Figure 2A). In the structure, an asymmetric unit contains one independent copy of the protein. The polypeptide chain was folded similarly to previously determined structures of oligopeptidases in intermediate conformations, including the structures of free SpOpBmod (PDB ID 7OB1) [15], free SpOpB-S532A (PDB ID 7ZJZ) [24], and TCK-bound SpOpBmod (PDB ID 7NE7) [23]. Comparison of the above structures gave RMSD values for Cα-atoms ranging from 0.3 to 0.8 Å, whereas comparison of the new structure with that of TCK-bound SpOpB in a closed conformation (PDB ID 7YWP) [17] gave an RMSD of 1.8 Å.

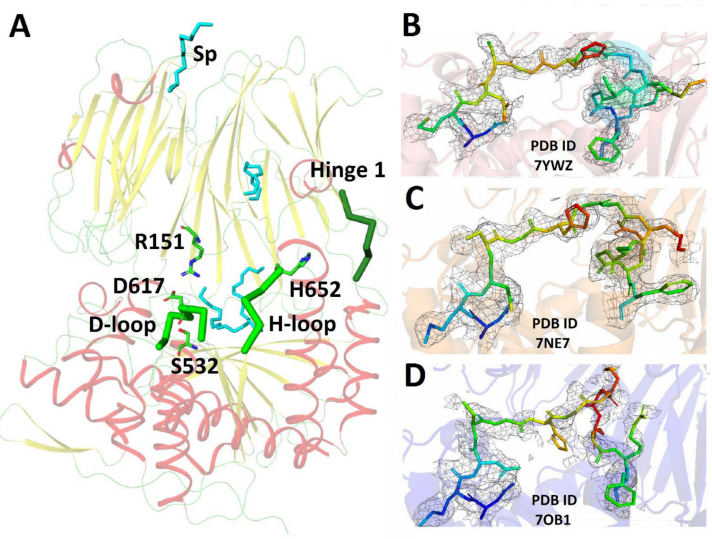

Figure 2. The crystal structure of SpOpBmod (PDB ID 7YWZ) is characterized by a typical polypeptide fold and improved electron density in the H-loop region. (**A**) Cartoon presentation of the crystal structure colored according to the secondary structure elements. Residues of the catalytic triad and R151 are shown in green sticks. Spermine molecules are shown in light blue sticks. The spermine, which participates in the formation of the crystal lattice, is designated Sp. The first hinge peptide and D- and H-loops (carrying the catalytic D and H residues) are colored in dark and light green, respectively. (**B**–**D**) Electron densities of the H-loops and their surroundings in the indicated the structures: SpOpBmod (**B**), SpOpBmod-TCK (**C**), and SpOpB-S532A (**D**). Residues are colored according to B-factor; the omitted Fo-Fc map is contoured at 1.5 Å RMSD.

Five spermine molecules were detected in the interdomain cavity of SpOpBmod, whereas one spermine molecule was located outside the interdomain cavity and participated in the crystal lattice formation (Figure 2A).

Similarly to the previously reported structures of the hinge-modified enzymes SpOpBmod [15,24] and SpOpBmod-TCK [23], in the new structure the catalytic D617 was stabilized between the other two residues of the catalytic triad by forming an interdomain salt bridge D617-R151 (Figure 2A). The distance between the guanidino and carboxyl groups of the corresponding residues was 2.77 Å. This salt bridge was absent in structures of enzymes with intact hinge regions crystallized in either intermediate or closed conformation (PDB ID 7ZJZ and 7YWP) [17,24]. This salt bridge appears to be one of the reasons for the loss of activity observed for the enzyme with a modified hinge region (see Section 3.3 for a detailed explanation). It is interesting to note that the model of SpOpB in the closed conformation obtained by homology modeling using the structures of antipain-bound protozoan OpBs (PDB ID 4BP9 and 2XE4, [14,16]) as starting structures, as well as their invariants obtained by MD simulations, contained this bridge [43,44], whereas this bridge was absent in the model of SpOpB built by the AlphaFold2 [45] (https://www.uniprot.org/uniprotkb/B3VI58/ accessed on 1 October 2023).

The new structure had obvious electron density for the mobile H-loop residues (Figure 2B). In previously determined SpOpBmod structures (e.g., PDB ID 7OB1), the electron density of the H-loop residues was poor or absent. The only exception was the structure of the SpOpBmod-TCK complex (PDB ID 7NE7), in which one of the two TCK molecules was covalently bound to the catalytic H652 and thereby fixed the position of H652 and neighboring residues, forming the H-loop. Figure 2 shows a comparison of the electron densities of the H-loop residues in the reported structure (Figure 2B) and in the previously obtained structures mentioned above (Figure 2C,D). It can be seen that in the new structure the electron density of the H-loop is of even better quality than in the SpOpBmod-TCK structure. Although the electron density of the imidazole ring of catalytic H652 is still missing.

Thus, the new structure of SpOpBmod and the structure of the SpOp-Bmod-TCK complex were selected for comparative analysis of interdomain interactions in the intermediate conformation of SpOpBmod together with the reference structure of SpOpB-S532A, in which the first hinge peptide was native.

3.2. Generation of the Model of the Open Conformation of SpOpBmod Using MD Simulations Combined with the SAXS Experiment

Previously, SAXS experiments showed that the open conformation predominates in solutions of both enzymes (SpOpB and SpOpBmod) [15]. However, the crystal structures of these enzymes in the open conformation could not be obtained, which was due to the fact that both variants of the enzyme could be crystallized only in the presence of spermine, which in turn caused the enzymes transition to an intermediate conformation [15].

It is well known that the combination of computational predictions (modeling, docking and MD) with the results of experimental methods of structural biology (SAXS, NMR and neutron scattering) can significantly improve the quality of predicted structures for various biological macromolecules and macromolecular systems [46–48]. Due to the lack of an experimentally obtained structure, we decided to construct a reliable model of SpOpBmod in the open conformation using a hybrid algorithm combining molecular dynamics (MD) simulations with SAXS experiment.

This hybrid algorithm consisted of several steps. We first used MD simulations to generate a set of different structural invariants for all three conformations of SpOpBmod. These structural invariants were then used to calculate SAXS curves. Finally, comparison of the calculated SAXS curves with the experimental SAXS curve made it possible to select the most probable structural invariant. The algorithm used can be applied to study the dynamics of a wide range of proteins.

When comparing experimental and model SAXS curves, in addition to χ^2 and Rg values, we analyzed a number of other parameters, including the inter-domain distance (Did), Dmax, and Rg of separated domains (R1g and R2g) (Table 2 and Figure 3).

As expected, based on the χ^2 and Rg values, the SAXS curves calculated for both the starting model of the open conformation and for the structural invariants generated along the MD trajectory demonstrated the best fit to the experimental SAXS curve (Table 2).

Figure 3A shows a plot of the χ^2 values calculated by fitting SAXS curves of structural invariants generated during the simulation of the starting model of the SpOpBmod open conformation with the experimental SAXS curve. Analysis of the structural invariants along the MD trajectory shows that the best-fitted models accumulate at the beginning of the trajectory. In this regard, a time interval around 20 ns was analyzed in detail (inset in Figure 3A). The minimum value of χ^2 (2.85) corresponds to the structural invariant (SpOpBmodOpen) generated at 19.9 ns of the MD trajectory.

The best structural invariant (SpOpBmodOpen) was selected for comparative analysis of interdomain interactions in the open conformation of SpOpBmod, while a model of the open conformation of SpOpB with an intact hinge region (SpOpBopen), obtained using a combination of classical MD dynamics and essential sampling in a previous study [24], was used as the reference structure.

Figure 3B shows the time development of structural characteristics of SpOpBmod in the open conformation during MD simulation, such as Rg, Did, R1g, and R2g. According to the R1g and R2g values, the sizes of individual domains did not change within the limits of calculation errors. This indicates that the decrease in Rg values is associated exclusively with the decrease in Did values observed as the domains approach each other. This fact can be considered as an illustration of the postulate that the conformational transitions of OpBs (as well as other POPs) are the result of the convergence and divergence of domains, while the domains themselves can be considered as solid globular structures with local conformational changes that are beyond the sensitivity of SAXS.

Table 2. Comparison of the experimental SAXS curve obtained for SpOpBmod with model SAXS curves calculated for the three major conformations of SpOpBmod.

Sample Description		χ^2	Rg, nm (ΔRg = ±0.03 nm)	Dmax, nm (ΔDmax = ±0.1 nm)	Did, nm (ΔDid = ±0.01 nm)	R1g and R2g, nm (ΔRg = ±0.03 nm)	
						R1g	R2g
Data from experimental SAXS curve							
Solution			2.76	8.7			
Data from model SAXS curves calculated for starting structures							
Open conformation		3.36	2.78	8.7	3.69	2.04	2.14
Intermediate conformation		18.12	2.64	7.9	3.23	2.01	2.12
Closed conformation		31.62	2.57	7.9	3.05	2.00	2.11
Data from model SAXS curves calculated for structures derived from MD experiments							
Open	t = 0 ns	3.49	2.79	8.7	3.69	2.05	2.14
	Main cluster *	17.20	2.68	8.2	3.32	2.03	2.16
	t = 10 ns	3.37	2.75	8.2	3.58	2.04	2.14
	t = 20 ns	2.97	2.76	8.3	3.61	2.03	2.15
	t = 30 ns	7.82	2.71	8.4	3.42	2.03	2.17
	t = 40 ns	4.87	2.72	8.2	3.46	2.03	2.16
	t = 50 ns	10.42	2.70	8.4	3.38	2.02	2.17
	t = 60 ns	15.38	2.67	8.5	3.32	2.03	2.14
	t = 70 ns	17.56	2.66	8.1	3.30	2.04	2.15
	t = 80 ns	17.88	2.67	8.3	3.33	2.04	2.15
	t = 90 ns	17.60	2.67	8.1	3.32	2.03	2.15
	t = 100 ns	16.22	2.66	8.4	3.29	2.02	2.15
	Best structure (SpOpBmodOpen)						
	t = 19.9 ns	2.85	2.75	8.4	3.57	2.03	2.16
Intermediate	t = 0 ns	18.12	2.64	7.9	3.23	2.01	2.12
	Main cluster *	19.23	2.67	8.3	3.28	2.04	2.14
Closed	t = 0 ns	31.62	2.57	7.9	3.05	2.00	2.11
	Main cluster *	28.96	2.61	8.0	3.15	2.03	2.14

* The main clusters cover 35–45% of the MD trajectories and have RMSD between structures of 1–1.2 Å.

3.3. Comparison of Interdomain Interactions in Intermediate and Open Conformations of SpOpB with Intact and Modified Hinge Regions

We have previously shown that modification of the first hinge peptide leads to strong inactivation of the enzyme [15]. Moreover, we have shown that this modification is associated with the formation of an interdomain salt bridge D617-R151. This SB involves the catalytic residue D617 causing its stabilization in a position that prevents the movement of the H-loop and the catalytic H652 itself towards the catalytic S532, which is necessary for the assembly of the catalytic triad and for catalytic activation of the enzyme [24]. Since there are no direct contacts between the hinge region and the catalytic residues, this effect must be associated with a series of local rearrangements, more precisely, with rearrangements of the local network of interdomain contacts.

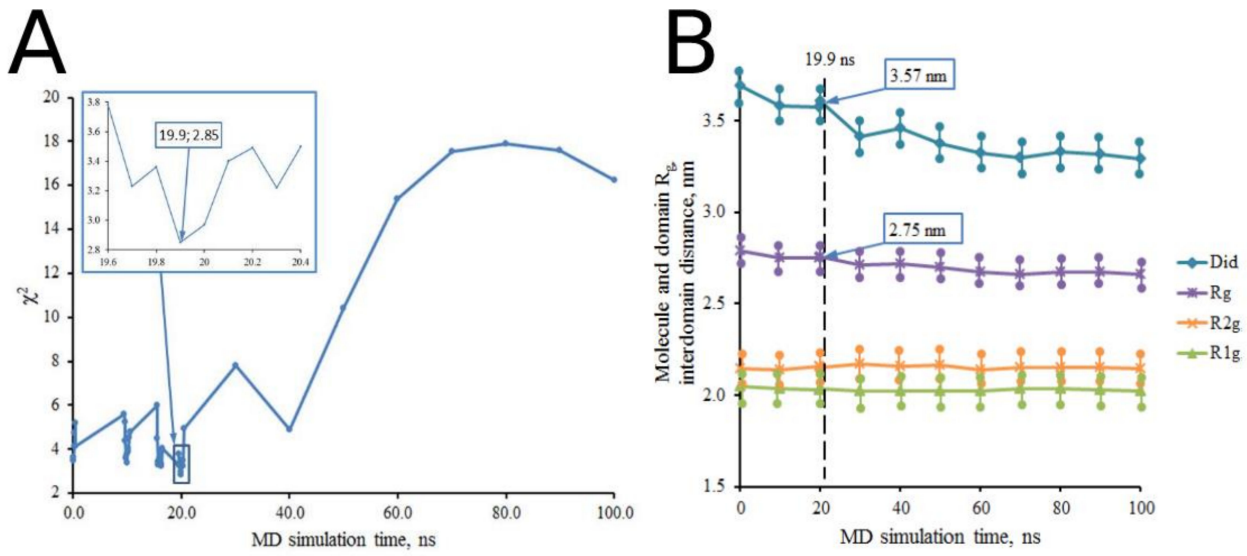

Figure 3. Evaluation of structural invariants generated during MD simulation of SpOpBmod in the open conformation. (**A**) Time-dependent development of reduced chi-square (χ^2) values calculated by comparing model SAXS curves with the experimental one. The inset shows a time fragment when the best model (with χ^2 = 2.85) was generated at 19.9 ns of the MD trajectory. (**B**) Time-dependent development of structural characteristics of the open conformation invariants generated during the simulation: the inter domain distance (Did), radius of gyration (Rg) of the entire molecule, and Rg of individual domains (R1g and R2g). The marking line corresponds to the structural characteristics of the best model.

To compare interdomain contacts in enzymes with intact and modified hinge regions, we used the crystal structures of SpOpB-S532A (PDB ID 7ZJZ), SpOpBmod (PDB ID 7YWZ), and SpOpBmod-TCK (PDB ID 7NE7) in intermediate conformations (Table 3). In addition, the comparison included a model of SpOpBmod in an open conformation (SpOpBmodOpen), obtained as described in Section 3.2, and a model of wild-type SpOpB in the open conformation (SpOpBopen), obtained using the combination of classical MD dynamics and essential sampling in [24] (Table 4).

The tables contain the information about both the polar contacts between two domains and the locations of interacting residues in the catalytic and β-propeller domains (e.g., secondary structure elements and propeller blades). Hinge peptides were assigned to the propeller domain; thus, multiple contacts between two adjacent hinge peptides were excluded from the analysis. Interdomain interactions were analyzed in the same order as they are presented in the tables: from the first hinge peptide, through β-propeller blades 1 to 7, and to the second hinge peptide. To clarify the following discussion, views of each domain from the interdomain cavity with secondary structure elements labeled are shown in Figure 1.

We first compared the interdomain interfaces in the crystal structures of free and TCK-bound SpOpBmod in the intermediate conformation. As noted in Section 3.1, the electron density made it possible to visualize and compare H-loops in both structures (Figure 2B,C). According to Table 3, the polar contacts between the two domains in both structures were almost identical, with the exception of differences associated with the presence of the TCK molecule covalently bound to H652 in the SpOpB-TCK structure. The H652-bound TCK did not allow the K655 side chain to occupy the same position as in the structure of free SpOpBmod. This difference led to the absence of several interdomain hydrogen bonds (H-bonds), including those between the K655 side chain and the main chains of residues E92, P93, and N95 of the β5-strand and the loop between the β5- and β6-strands of the first β-propeller blade. At the same time, the H-bonds of the main chain of K655 and the main and side chains of neighboring S656 with the main and side chains of E96 (also located in

the β5/β6-loop of the β-propeller) remained unchanged in both structures, leveling out the absence of the above-mentioned H-bonds in the SpOpB-TCK structure. As a result, the interdomain interfaces in the region adjacent to the first hinge peptide in the SpOpBmod and SpOpBmod-TCK structures turned out to be almost identical, indicating that both tertiary folds observed in the crystalline states are the result of the internal conformational dynamics of SpOpBmod, which was subsequently captured via inhibitor binding in the SpOpBmod-TCK structure.

Table 3. Hydrogen bonds and salt bridges connecting two domains in crystal structures of SpOpBmod (PDB ID 7YWZ), SpOpBmod-TCK (PDB ID 7NE7) and SpOpB-S532A (PDB ID 7ZJZ) in intermediate conformations.

Crystal Structures Domains		**SpOpBmod (7YWZ)**		**SpOpB-S532A (7ZJZ)**		**SpOpBmod-TCK (7NE7)**	
Propeller	**Catalytic**	**Atom 1 prop.**	**Atom 2 cat.**	**Atom 1 prop.**	**Atom 2 cat.**	**Atom 1 prop.**	**Atom 2 cat.**
Hinge1	α2	E71N	V68O	I71N	V68O	E71N	V68O
β5/β6, Blade 1	H-loop (α12)	E92O P93O N95O *E96OE2* E96OE2 E96O E96OE2 E96OE2	(K655NZ) (K655NZ) (K655NZ) *H652ND1* (K655N) (K655N) (S656N) (S656OG)	E96O E96O Y97OH	S656OG (R658NH2) S656N	*E96OE2* E96OE2 E96O E96OE2 E96OE1	*H652NE2* (K655N) (K655N) (S656N) (S656OG)
Blade 1/ Blade 2				A121O R124O	K655NZ K655NZ		
β9/β10, Blade 2		S149OG S149OG	S650O G651O			S149OG	S650O
	D-loop	*R151NH1*	*D617OD2*			*R151NH2*	*D617OD1*
β17/β18, Blade 4	α8/α9	T244OG1	D578OD2	T244OG1	D578OD2		
Blade 4/ Blade 5		*K269NZ*	*D578OD1/2*			*K269NZ*	*D578OD1/2*
β21/β22, Blade 5	α5	*K291NZ* N292OD1	*E494OE1/2* Q490N	*K291NZ* N292OD1	*E494OE1/2* Q490N	*K291NZ* N292OD1	*E494OE1* Q490N
β24, Blade 6		M317SD	Q490N	M317SD	Q490N	M317SD	Q490N
β25/β26, Blade 6	β34/α4	*R333NH1/2*	*D460OD1/2*	*R333NH1/2*	*D460OD1/2*	*R333NH1/2*	*D460OD1/2*
	β32	G336O	R418NH1	G336O	R418NH1	G336O	R418NH1
Blade 6/ Blade 7	β34/α4	T361N/OG1	P461O	T361N/OG1	P461O	T361N/OG1	P461O
β29/β30, Blade7		S380OG	F463N	S380OG	F463N	S380OG	F463N
	β33	M382SD	L433N	M382SD	L433N	M382SD	L433N
Hinge2	α2	K407N	R70O	K407N	R70O	K407NE	R70O
	η6	T410O	N413N	T410O T410OG1	N413N N413ND2	T410O	N413N

Salt bridges are shown in italics.

Table 4. Hydrogen bonds and salt bridges connecting two domains in the open conformation models of SpOpB and SpOpBmod.

Models / **Domains**		**SpOpBmodOpen**		**SpOpBopen**	
Propeller	**Catalytic**	**Atom 1 prop.**	**Atom 2 cat.**	**Atom 1 prop.**	**Atom 2 cat.**
β21/β22, Blade 5	α5 (β35/α5)	*K291NZ* N292ND2 N292OD1 N292OD1	*E494OE2* (L488O) Q490N L491N	*K291NZ* K291O N292OD1 N292OD1	*E494OE1* Q490NE2 Q490N L491N
β25, Blade 6	β34/α4 (β35/α5)	*R333NH1/2* R333NH1	*D460OD1/2* (E487O)	*R333NH1/2* R333NH2 R333NH1	*D460OD1/2* S458OG (E487O)
Blade 6/ Blade 7	β32	E335O T359OG1	R418NH1/2 S416OG	D357OD1	S416OG
	β34/α4	T361N/OG1	P461O	T361N/OG1	P461O
β29/β30, Blade7		S380O/OG M382SD M382SD	F463N A462N R467NH1	S380OG	F463N
Hinge2	α2 N-loop	K407N K407O N408O/OD1	R70O R70NE R70NH1	K407N K407O N408O	R70O R70NE R70NH1
	η6 N-loop	T410O T410OG1	N413N N412N	T410OG1	N412N

Salt bridges are shown in italics.

Further comparison of the hinge-modified SpOpBmod structures with the SpOpB-S532A structure with a native hinge peptide revealed noticeably differences of interdomain contacts both in regions adjacent to the first hinge peptide and in regions more distant from it (Table 3). The immediate surroundings of the first hinge peptide included the preceding and subsequent polypeptide chains as well as the second hinge peptide (Figure 1). The β5-strand and β5/β6-loop from the first blade of the β-propeller—as well as the N-terminus of the C-terminal α12-helix, which is preceded by the C-terminus of the H-loop—can also be included there (Figure 4).

According to Table 3, in the SpOpB-S532A structure, the side chain of K655 from the H-loop formed H-bonds with the main chains of residues A121 and R124 from the α3-helix and the following α3/β8-loop, which connected the first and second blades of the β-propeller. The side chains of S656 from the H-loop and R658 from the α12-helix formed H-bonds with the main chain of E96 from the β5/β6-loop of the β-propeller, whereas the main chain of S656 formed an H-bond with the side chain of Y97 from the same loop. All these contacts differed from those observed in the structures of the hinge-modified enzymes (see Table 3).

The described above differences in the immediate spatial surroundings of the first hinge peptide led to the rearrangement of the interdomain interface in more distant regions. According to Table 3, in the SpOpB-S532A structure, there were no polar contacts between the second propeller blade and the catalytic domain, whereas in both SpOpBmod structures, the main chain of S650 from the H-loop formed an H-bond with the side chain of S149 from the β9/β10-loop of the second β-propeller blade. This contact contributed to the convergence of the β9/β10-loop with the D-loop, which in turn was adjacent to the H-loop. Figure 1 shows that the D- and H-loops are topologically related to each other, as they follow two adjacent parallel β-strands (β38 and β39) from a curved β-sheet that serves as the core of the α/β-hydrolase fold of the catalytic domain. In turn, the proximity of the β9/β10-loop to the D-loop allows residues R151 and D617 to approach each other to form SB. Thus, in the both SpOpBmod and SpOpBmod-TCK structures, catalytic D617

is stabilized in its positions by the interdomain SB D617-R151, which complicates the rearrangement of the catalytic triad required for catalytic activation but facilitates the crystallization of hinge-modified enzyme [15,24].

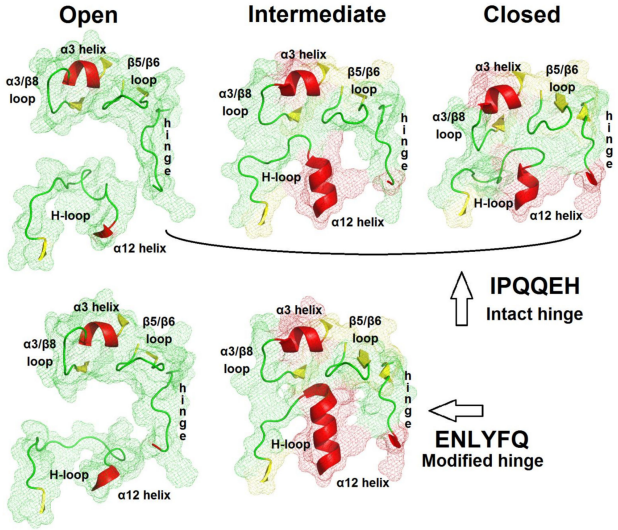

Figure 4. Cartoon mesh presentation of secondary structure elements from the β-propeller and catalytic domains that surround the first hinge peptide (hinge) in different conformations of SpOpB. The α-helices, β-strands, and loops are colored in red, yellow, and green, respectively. Molecular models of SpOpBopen and SpOpBmodOpen were used to prepare images of the open conformation; crystal structures of SpOpBmod, SpOpB-S532A, and SpOpB-TCK—for preparing images of the intermediate and closed conformations, respectively.

Despite the differences in interdomain interfaces found in the structures of the intermediate conformations of enzymes with intact and modified hinges, comparison of the structures of open conformations of the same enzymes modeled using a combination of MD simulations with experimental SAXS data revealed similar interdomain interfaces (Table 4). In both cases (SpOpB and SpOpBmod in open conformations), the interdomain interfaces were formed only by the propeller blades 5–7 and the secondary structure elements (mainly loops) of the catalytic domain located opposite. At the same time, the number of polar contacts between the contacting regions even increased (Table 4).

Figure 4 allows us to compare the relative positions of the secondary structure elements of the β-propeller and catalytic domains surrounding the first hinge peptide in different conformations. The same crystal structures and structural models that were used for the comparative analysis of the interdomain interface were taken, but the hinge-modified enzyme in the intermediate conformation was presented only by the SpOpBmod structure. The crystal structure of the closed conformation obtained for SpOpB in complex with TCK (PDB ID 7YWP) [17] was added to the comparison.

According to Figure 4, in open conformations, there are no interdomain contacts in the immediate surroundings of the first hinge peptide and the hinge modification does not cause significant differences. At the same time, as the domains approach each other, the modification promotes accelerated structuring of the first hinge peptide. This structuring results in the formation of a short β-strand from residues 75–76, which in turn causes elongation of the adjacent β5-strand of the first β-propeller blade. In the hinge-modified enzyme, the β5/β6 loop of the first blade approaches the catalytic domain earlier (at a lower degree of domain convergence) than in a protein with an intact hinge. This leads to the formation of numerous interdomain contacts between the β5/β6 loop of the first β-propeller blade and residues of the catalytic domain. As a result, an abnormal elongation of the α12 helix and shortening of the H-loop occurs (Figure 4).

The boundary between the H-loop and the α12-helix passed through residues 661/662 in the open conformation models (the shortest α12-helix), residues 656/657 in the SpOpB-

S532A structure (the α12-helix extended by 5 residues), and residues 652/653 in structures of the hinge-modified enzyme (the α12-helix extended by nine residues). The beginning of the H-loop in all cases corresponds to residue 648.

This elongation of the α12-helix leads to the loss of contacts of the shortened H-loop with α3-helix and α3/β8-loop (transition between the first and second β-propeller blades), instead of which the remaining part of the H-loop and the adjacent D-loop interact with residues of the β8/β9-loop of the second β-propeller blade (Table 3).

In an enzyme with a native hinge, structuring of the first hinge peptide occurs only at the maximum degree of domain closure (in a closed conformation), and elongation of the α12-helix leading to shortening of the H-loop occur to a much lesser extent (Figure 4). Based on this, we can conclude that the interdomain interface observed in the structures of hinge-modified enzymes can be considered an extreme version of the H-loop rearrangement, in which the approach of the domains does not lead to the assembly of the catalytic triad. However, the intermediate conformation observed in the structure of the enzyme with an intact hinge peptide (SpOpB-S532A) illustrates the productive transition between open and closed conformations.

4. Conclusions

Here we report a new crystal structure of hinge-modified oligopeptidase B from *Serratia proteamaculans* in an intermediate conformation with improved electron density in the mobile H-loop region. Comparison of this structure with the structure of SpOpBmod in complex with TCK carried out in this work shows that both tertiary folds observed in crystalline states result from the internal conformational dynamics of SpOpBmod, which were captured via inhibitor binding into the structure of the SpOpB-TCK complex. In addition, the SAXS study of SpOpBmod in solution made it possible to determine the structural parameters of the open conformation of SpOpBmod and create a corresponding model. This model was subjected to comparative analysis together with the crystal structures discussed above and previously reported structures of SpOpB with native hinges in different conformations.

As a result, it was found that the interdomain interface observed in the SpOpBmod structures can be considered as a certain extreme version of the H-loop arrangement, in which the convergence of domains does not lead to the assembly of the catalytic triad. However, the intermediate conformation observed in the structure of the enzyme with a native hinge illustrates the productive transition between the open and closed conformation. The obtained results illustrate the role of the hinge region in SpOpB conformational transitions and provide a structural explanation for why hinge-modified SpOpB lost its enzymatic activity.

Author Contributions: Conceptualization, A.G.M., V.I.T., Y.A.G. and T.V.R.; methodology, Y.A.G., D.E.P. and V.I.T.; software, V.I.T., D.E.P. and Y.A.G.; validation, V.I.T., D.E.P. and Y.A.G.; formal analysis, A.G.M.; investigation, A.Y.N., D.E.P., Y.A.G., Y.K.A. and G.S.P.; resources, T.V.R. and G.S.P.; data curation, D.E.P., V.I.T., A.G.M., Y.A.G. and T.V.R.; writing—original draft preparation, Y.A.G. and T.V.R.; writing—review and editing, V.I.T., Y.A.G. and T.V.R.; visualization, V.I.T., D.E.P. and Y.A.G.; supervision, T.V.R.; project administration, T.V.R.; funding acquisition, T.V.R. All authors have read and agreed to the published version of the manuscript.

Funding: The research was funded by the Russian Science Foundation, grant number 21-74-20154, https://rscf.ru/en/project/21-74-20154/ accessed on 1 October 2023 (in part of the preparation and characterization of the protein samples and the X-ray diffraction analysis). The work was also partially supported by the Ministry of Science and Higher Education of the Russian Federation within the State assignment to NRC Kurchatov Institute (in part of processing SAXS data) and to FSRC "Crystallography and Photonics" RAS (in a part of formal analysis). The upgraded "BioMUR" beamline is a part of the unique scientific facility of the Kurchatov Synchrotron Radiation Source supported by the Ministry of Science and Higher Education of the Russian Federation (project code RFMEFI61917X0007).

Data Availability Statement: The structural data used in this work is available in the RCSB Protein Data Bank (https://www.rcsb.org/, accessed on 1 October 2023): SpOpBmod (PDB ID 7YWZ), SpOpBmod-TCK (PDB ID 7NE7), SpOpB-S532A (PDB ID 7ZJZ), and SpOpB-TCK (7YWP).

Acknowledgments: We acknowledge the Center for collective use of "Bioorganika" of the Shemyakin-Ovchinnikov Institute of Bioorganic Chemistry RAS for usage of computing resources and the Resource Center for Molecular and Cellular Biology of the NRC "Kurchatov Institute" for providing the protein crystallization facility.

Conflicts of Interest: The authors declare no conflict of interest.

References

1. Allen, F.H.; Taylor, R. Librarians, Crystal Structures and Drug Design. *Chem. Commun.* **2005**, *41*, 5135–5140. [CrossRef]
2. Anderson, A.C. The Process of Structure-Based Drug Design. *Chem. Biol.* **2003**, *10*, 787–797. [CrossRef] [PubMed]
3. Ferguson, F.M.; Gray, N.S. Kinase Inhibitors: The Road Ahead. *Nat. Rev. Drug Discov.* **2018**, *17*, 353–377. [CrossRef] [PubMed]
4. Cohen, P.; Cross, D.; Jänne, P.A. Kinase Drug Discovery 20 Years after Imatinib: Progress and Future Directions. *Nat. Rev. Drug Discov.* **2021**, *20*, 551–569. [CrossRef] [PubMed]
5. Miller, M.S.; Maheshwari, S.; McRobb, F.M.; Kinzler, K.W.; Amzel, L.M.; Vogelstein, B.; Gabelli, S.B. Identification of Allosteric Binding Sites for PI3Kα Oncogenic Mutant Specific Inhibitor Design. *Bioorganic Med. Chem.* **2017**, *25*, 1481–1486. [CrossRef] [PubMed]
6. Agapova, Y.K.; Altukhov, D.A.; Timofeev, V.I.; Stroylov, V.S.; Mityanov, V.S.; Korzhenevskiy, D.A.; Vlaskina, A.V.; Smirnova, E.V.; Bocharov, E.V.; Rakitina, T.V. Structure-Based Inhibitors Targeting the Alpha-Helical Domain of the Spiroplasma Melliferum Histone-like HU Protein. *Sci. Rep.* **2020**, *10*, 15128. [CrossRef]
7. Teilum, K.; Olsen, J.G.; Kragelund, B.B. Protein Stability, Flexibility and Function. *Biochim. Biophys. Acta BBA-Proteins Proteom.* **2011**, *1814*, 969–976. [CrossRef] [PubMed]
8. Polgár, L. The Prolyl Oligopeptidase Family. *Cell. Mol. Life Sci. CMLS* **2002**, *59*, 349–362. [CrossRef]
9. Rawlings, N.D.; Barrett, A.J.; Thomas, P.D.; Huang, X.; Bateman, A.; Finn, R.D. The MEROPS Database of Proteolytic Enzymes, Their Substrates and Inhibitors in 2017 and a Comparison with Peptidases in the PANTHER Database. *Nucleic Acids Res.* **2018**, *46*, D624–D632. [CrossRef]
10. Rea, D.; Fülöp, V. Structure-Function Properties of Prolyl Oligopeptidase Family Enzymes. *Cell Biochem. Biophys.* **2006**, *44*, 349–365. [CrossRef]
11. Fülöp, V.; Böcskei, Z.; Polgár, L. Prolyl Oligopeptidase: An Unusual β-Propeller Domain Regulates Proteolysis. *Cell* **1998**, *94*, 161–170. [CrossRef]
12. Shan, L.; Mathews, I.I.; Khosla, C. Structural and Mechanistic Analysis of Two Prolyl Endopeptidases: Role of Interdomain Dynamics in Catalysis and Specificity. *Proc. Natl. Acad. Sci. USA* **2005**, *102*, 3599–3604. [CrossRef]
13. Li, M.; Chen, C.; Davies, D.; Chiu, T. Induced-Fit Mechanism for Prolyl Endopeptidase. *J. Biol. Chem.* **2010**, *285*, 21487–21495. [CrossRef] [PubMed]
14. Canning, P.; Rea, D.; Morty, R.E.; Fülöp, V. Crystal Structures of Trypanosoma Brucei Oligopeptidase B Broaden the Paradigm of Catalytic Regulation in Prolyl Oligopeptidase Family Enzymes. *PLoS ONE* **2013**, *8*, e79349. [CrossRef] [PubMed]
15. Petrenko, D.E.; Timofeev, V.I.; Britikov, V.V.; Britikova, E.V.; Kleymenov, S.Y.; Vlaskina, A.V.; Kuranova, I.P.; Mikhailova, A.G.; Rakitina, T.V. First Crystal Structure of Bacterial Oligopeptidase B in an Intermediate State: The Roles of the Hinge Region Modification and Spermine. *Biology* **2021**, *10*, 1021. [CrossRef] [PubMed]
16. McLuskey, K.; Paterson, N.G.; Bland, N.D.; Isaacs, N.W.; Mottram, J.C. Crystal Structure of Leishmania Major Oligopeptidase B Gives Insight into the Enzymatic Properties of a Trypanosomatid Virulence Factor*. *J. Biol. Chem.* **2010**, *285*, 39249–39259. [CrossRef] [PubMed]
17. Petrenko, D.E.; Karlinsky, D.M.; Gordeeva, V.D.; Arapidi, G.P.; Britikova, E.V.; Britikov, V.V.; Nikolaeva, A.Y.; Boyko, K.M.; Timofeev, V.I.; Kuranova, I.P.; et al. Crystal Structure of Inhibitor-Bound Bacterial Oligopeptidase B in the Closed State: Similarity and Difference between Protozoan and Bacterial Enzymes. *Int. J. Mol. Sci.* **2023**, *24*, 2286. [CrossRef]
18. Haffner, C.D.; Diaz, C.J.; Miller, A.B.; Reid, R.A.; Madauss, K.P.; Hassell, A.; Hanlon, M.H.; Porter, D.J.T.; Becherer, J.D.; Carter, L.H. Pyrrolidinyl Pyridone and Pyrazinone Analogues as Potent Inhibitors of Prolyl Oligopeptidase (POP). *Bioorganic Med. Chem. Lett.* **2008**, *18*, 4360–4363. [CrossRef]
19. Kaushik, S.; Etchebest, C.; Sowdhamini, R. Decoding the Structural Events in Substrate-Gating Mechanism of Eukaryotic Prolyl Oligopeptidase Using Normal Mode Analysis and Molecular Dynamics Simulations. *Proteins Struct. Funct. Bioinform.* **2014**, *82*, 1428–1443. [CrossRef]
20. Kichik, N.; Tarrago, T.; Claasen, B.; Gairi, M.; Millet, O.; Giralt, E. 15N Relaxation NMR Studies of Prolyl Oligopeptidase, an 80 KDa Enzyme, Reveal a Pre-Existing Equilibrium between Different Conformational States. *Chembiochem Eur. J. Chem. Biol.* **2011**, *12*, 2737–2739. [CrossRef]
21. Szeltner, Z.; Rea, D.; Juhász, T.; Renner, V.; Fülöp, V.; Polgár, L. Concerted Structural Changes in the Peptidase and the Propeller Domains of Prolyl Oligopeptidase Are Required for Substrate Binding. *J. Mol. Biol.* **2004**, *340*, 627–637. [CrossRef]

22. Ellis-Guardiola, K.; Rui, H.; Beckner, R.L.; Srivastava, P.; Sukumar, N.; Roux, B.; Lewis, J.C. Crystal Structure and Conformational Dynamics of Pyrococcus Furiosus Prolyl Oligopeptidase. *Biochemistry* **2019**, *58*, 1616–1626. [CrossRef] [PubMed]
23. Timofeev, V.I.; Petrenko, D.E.; Agapova, Y.K.; Vlaskina, A.V.; Karlinsky, D.M.; Mikhailova, A.G.; Kuranova, I.P.; Rakitina, T.V. The Crystal Structure of Nα-p-Tosyl-Lysyl Chloromethylketone-Bound Oligopeptidase B from Serratia Proteamaculans Revealed a New Type of Inhibitor Binding. *Crystals* **2021**, *11*, 1438. [CrossRef]
24. Britikov, V.V.; Timofeev, V.I.; Petrenko, D.E.; Britikova, E.V.; Nikolaeva, A.Y.; Vlaskina, A.V.; Boyko, K.M.; Mikhailova, A.G.; Rakitina, T.V. Elucidation of the Conformational Transition of Oligopeptidase B by an Integrative Approach Based on the Combination of X-Ray, SAXS, and Essential Dynamics Sampling Simulation. *Crystals* **2022**, *12*, 712. [CrossRef]
25. Petrenko, D.E.; Nikolaeva, A.Y.; Lazarenko, V.A.; Dorovatovskii, P.V.; Timofeev, V.I.; Vlaskina, A.V.; Korzhenevskiy, D.A.; Mikhailova, A.G.; Rakitina, T.V. Screening of Conditions That Facilitate Crystallization of Oligopeptidase B from Serratia Proteamaculans by Differential Scanning Fluorimetry. *Crystallogr. Rep.* **2020**, *65*, 264–268. [CrossRef]
26. Battye, T.G.G.; Kontogiannis, L.; Johnson, O.; Powell, H.R.; Leslie, A.G.W. iMOSFLM: A New Graphical Interface for Diffraction-Image Processing with MOSFLM. *Acta Crystallogr. D Biol. Crystallogr.* **2011**, *67*, 271–281. [CrossRef]
27. Long, F.; Vagin, A.A.; Young, P.; Murshudov, G.N. BALBES: A Molecular-Replacement Pipeline. *Acta Crystallogr. D Biol. Crystallogr.* **2008**, *64*, 125–132. [CrossRef] [PubMed]
28. Murshudov, G.N.; Skubák, P.; Lebedev, A.A.; Pannu, N.S.; Steiner, R.A.; Nicholls, R.A.; Winn, M.D.; Long, F.; Vagin, A.A. REFMAC5 for the Refinement of Macromolecular Crystal Structures. *Acta Crystallogr. D Biol. Crystallogr.* **2011**, *67*, 355–367. [CrossRef] [PubMed]
29. Emsley, P.; Lohkamp, B.; Scott, W.G.; Cowtan, K. Features and Development of Coot. *Acta Crystallogr. D Biol. Crystallogr.* **2010**, *66*, 486–501. [CrossRef] [PubMed]
30. Krissinel, E.; Henrick, K. Inference of Macromolecular Assemblies from Crystalline State. *J. Mol. Biol.* **2007**, *372*, 774–797. [CrossRef] [PubMed]
31. Collaborative Computational Project, Number 4 The CCP4 Suite: Programs for Protein Crystallography. *Acta Crystallogr. D Biol. Crystallogr.* **1994**, *50*, 760–763. [CrossRef] [PubMed]
32. Diederichs, K.; Karplus, P.A. Improved R-Factors for Diffraction Data Analysis in Macromolecular Crystallography. *Nat. Struct. Biol.* **1997**, *4*, 269–275. [CrossRef] [PubMed]
33. Manalastas-Cantos, K.; Konarev, P.V.; Hajizadeh, N.R.; Kikhney, A.G.; Petoukhov, M.V.; Molodenskiy, D.S.; Panjkovich, A.; Mertens, H.D.T.; Gruzinov, A.; Borges, C.; et al. ATSAS 3.0: Expanded Functionality and New Tools for Small-Angle Scattering Data Analysis. *J. Appl. Crystallogr.* **2021**, *54*, 343–355. [CrossRef] [PubMed]
34. Hammersley, A.P.; Svensson, S.O.; Hanfland, M.; Fitch, A.N.; Hausermann, D. Two-Dimensional Detector Software: From Real Detector to Idealised Image or Two-Theta Scan. *High Press. Res.* **1996**, *14*, 235–248. [CrossRef]
35. Abraham, M.J.; Murtola, T.; Schulz, R.; Páll, S.; Smith, J.C.; Hess, B.; Lindahl, E. GROMACS: High Performance Molecular Simulations through Multi-Level Parallelism from Laptops to Supercomputers. *SoftwareX* **2015**, *1*, 19–25. [CrossRef]
36. Lindorff-Larsen, K.; Piana, S.; Palmo, K.; Maragakis, P.; Klepeis, J.L.; Dror, R.O.; Shaw, D.E. Improved Side-Chain Torsion Potentials for the Amber Ff99SB Protein Force Field. *Proteins Struct. Funct. Bioinform.* **2010**, *78*, 1950–1958. [CrossRef]
37. Berendsen, H.J.C.; Postma, J.P.M.; van Gunsteren, W.F.; DiNola, A.; Haak, J.R. Molecular Dynamics with Coupling to an External Bath. *J. Chem. Phys.* **1984**, *81*, 3684–3690. [CrossRef]
38. Parrinello, M.; Rahman, A. Strain Fluctuations and Elastic Constants. *J. Chem. Phys.* **1982**, *76*, 2662–2666. [CrossRef]
39. York, D.M.; Darden, T.A.; Pedersen, L.G. The Effect of Long-Range Electrostatic Interactions in Simulations of Macromolecular Crystals: A Comparison of the Ewald and Truncated List Methods. *J. Chem. Phys.* **1993**, *99*, 8345–8348. [CrossRef]
40. Kabsch, W.; Sander, C. Dictionary of Protein Secondary Structure: Pattern Recognition of Hydrogen-Bonded and Geometrical Features. *Biopolymers* **1983**, *22*, 2577–2637. [CrossRef]
41. Franke, D.; Petoukhov, M.V.; Konarev, P.V.; Panjkovich, A.; Tuukkanen, A.; Mertens, H.D.T.; Kikhney, A.G.; Hajizadeh, N.R.; Franklin, J.M.; Jeffries, C.M.; et al. ATSAS 2.8: A Comprehensive Data Analysis Suite for Small-Angle Scattering from Macromolecular Solutions. *J. Appl. Crystallogr.* **2017**, *50*, 1212–1225. [CrossRef] [PubMed]
42. Svergun, D.I.; Feigin, L.A. *Structure Analysis by Small-Angle X-ray and Neutron Scattering*; Taylor, G.W., Ed.; Plenum Press: New York, NY, USA, 1987; ISBN 978-0-306-42629-2.
43. Mikhailova, A.G.; Rakitina, T.V.; Timofeev, V.I.; Karlinsky, D.M.; Korzhenevskiy, D.A.; Agapova, Y.K.; Vlaskina, A.V.; Ovchinnikova, M.V.; Gorlenko, V.A.; Rumsh, L.D. Activity Modulation of the Oligopeptidase B from Serratia Proteamaculans by Site-Directed Mutagenesis of Amino Acid Residues Surrounding Catalytic Triad Histidine. *Biochimie* **2017**, *139*, 125–136. [CrossRef] [PubMed]
44. Petrenko, D.; Mikhailova, A.; Timofeev, V.; Agapova, Y.; Karlinsky, D.; Komolov, A.; Korzhenevskiy, D.; Vlaskina, A.; Rumsh, L.; Rakitina, T. Molecular Dynamics Complemented by Site-Directed Mutagenesis Reveals Significant Difference between the Interdomain Salt Bridge Networks Stabilizing Oligopeptidases B from Bacteria and Protozoa in Their Active Conformations. *J. Biomol. Struct. Dyn.* **2019**, *38*, 4868–4882. [CrossRef] [PubMed]
45. Jumper, J.; Evans, R.; Pritzel, A.; Green, T.; Figurnov, M.; Ronneberger, O.; Tunyasuvunakool, K.; Bates, R.; Žídek, A.; Potapenko, A.; et al. Highly Accurate Protein Structure Prediction with AlphaFold. *Nature* **2021**, *596*, 583–589. [CrossRef]

46. Larsen, A.H.; Wang, Y.; Bottaro, S.; Grudinin, S.; Arleth, L.; Lindorff-Larsen, K. Combining Molecular Dynamics Simulations with Small-Angle X-Ray and Neutron Scattering Data to Study Multi-Domain Proteins in Solution. *PLoS Comput. Biol.* **2020**, *16*, e1007870. [CrossRef]
47. He, W.; Henning-Knechtel, A.; Kirmizialtin, S. Visualizing RNA Structures by SAXS-Driven MD Simulations. *Front. Bioinform.* **2022**, *2*, 781949. [CrossRef]
48. Bengtsen, T.; Holm, V.L.; Kjølbye, L.R.; Midtgaard, S.R.; Johansen, N.T.; Tesei, G.; Bottaro, S.; Schiøtt, B.; Arleth, L.; Lindorff-Larsen, K. Structure and Dynamics of a Nanodisc by Integrating NMR, SAXS and SANS Experiments with Molecular Dynamics Simulations. *eLife* **2020**, *9*, e56518. [CrossRef]